Promenading pairs of walking droplets: Dynamics and stability

Juncal Arbelaiz,[1] Anand U. Oza,[2] and John W. M. Bush[1,*]
[1]*Department of Mathematics, Massachusetts Institute of Technology, Cambridge, Massachusetts 02139, USA*
[2]*Department of Mathematical Sciences, New Jersey Institute of Technology, Newark, New Jersey 07102, USA*

(Received 26 June 2017; published 31 January 2018)

We present the results of an integrated experimental and theoretical investigation of the promenade mode, a bound state formed by a pair of droplets walking side by side on the surface of a vibrating fluid bath. Particular attention is given to characterizing the dependence of the promenading behavior on the vibrational forcing for drops of a given size. We also enumerate the different instabilities that may arise, including transitions to smaller promenade modes or orbiting pairs. Our theoretical developments highlight the importance of the vertical bouncing dynamics on the stability characteristics. Specifically, quantitative comparison between experiment and theory prompts further refinement of the stroboscopic model [A. U. Oza *et al.*, J. Fluid Mech. **737**, 552 (2013)] through inclusion of phase adaptation and reveals the critical role that impact phase variations play in the stability of the promenading pairs.

DOI: 10.1103/PhysRevFluids.3.013604

I. INTRODUCTION

Consider a vibrating fluid bath subject to a vertical acceleration $\Gamma = \gamma \cos(2\pi f t)$. Provided $\gamma < \gamma_F$, where γ_F is the Faraday threshold, the surface of the bath remains flat. Beyond γ_F, subharmonic Faraday waves arise, with a wavelength prescribed by the standard water-wave dispersion relation [1]. Walker [2] discovered that a millimetric droplet may bounce indefinitely on such a surface provided $\gamma > \gamma_B$, where $\gamma_B < \gamma_F$ is the bouncing threshold. Protière *et al.* [3] discovered that, for a limited parameter regime that depends on the fluid surface tension, viscosity, forcing frequency, and drop size, there exists a walking threshold γ_W such that $\gamma_B < \gamma_W < \gamma_F$, above which the bouncing state destabilizes into a walking regime. The droplet then self-propels through a resonant interaction with its own wave field, executing a form of pilot-wave dynamics [4]. When $\gamma_W \lesssim \gamma \ll \gamma_F$, the waves are quickly damped and the walking droplet, or walker, feels only the wave from the most recent impact. As $\gamma \to \gamma_F$ from below, the waves are more persistent and the walker's trajectory is influenced by its distant past. The resultant path memory [5,6] is prescribed in terms of the memory time $T_M = T_d/(1-\gamma/\gamma_F)$, where $T_d \approx (2\nu k_F^2)^{-1}$ is the decay time of waves with Faraday wavelength $\lambda_F = 2\pi/k_F$ in the absence of vibrational forcing and ν is the kinematic viscosity. Noting that T_M is a monotonically increasing function of γ/γ_F for $\gamma < \gamma_F$, we will henceforth refer to the ratio γ/γ_F as memory. The walker system is remarkable in that, in the high memory limit of $\gamma/\gamma_F \to 1$, it exhibits certain features previously thought to be exclusive to the quantum realm [5,7–9]. Its relation to quantum pilot-wave theories has been reviewed elsewhere [4,10,11].

For multiple-droplet systems, the global wave field is deduced from the superposition of the wave fields generated by the individual droplets. Through this global wave field, the droplets may interact and form bound states, such as lattices [12–14], orbiting pairs [3,15], and ratcheting pairs [16]. We here focus our attention on the promenading state [3], wherein a pair of identical droplets walks in

*bush@math.mit.edu

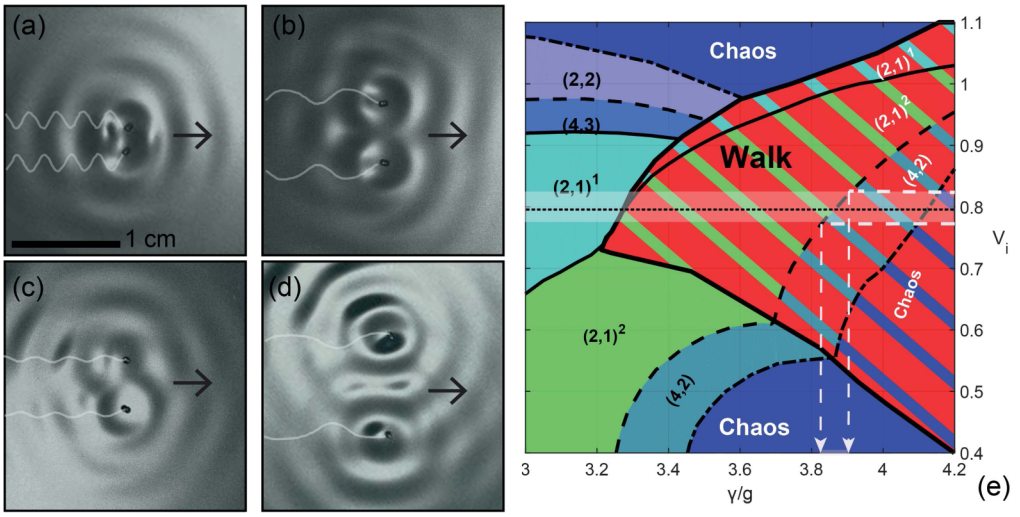

FIG. 1. Plan view of promenading pairs of order (a) $N = 1$, (b) $N = 2$, (c) $N = 1.5$, and (d) $N = 2.5$. The black arrows indicate the direction of motion and white lines the droplet trajectories. Note that the drops bounce in phase for integer N and out of phase for half-integer N. (e) Regime diagram [19] of different bouncing and walking states for single drops, for 20 cSt silicone oil, and vibrational frequency $f = 80$ Hz, as a function of the vibration number $V_i = 2\pi f\sqrt{\rho R^3/\sigma}$ and dimensionless forcing acceleration γ/g, where g is the gravitational acceleration. The walking regime is indicated in red, the bouncing regime in green and blue, and the Faraday threshold $\gamma_F = 4.2g$. The region shaded in white corresponds to a drop of radius $R = 0.38 \pm 0.01$ mm, for which $V_i = 0.793 \pm 0.032$. The dashed arrows indicate the range of forcing acceleration over which the transition from the $(2,1)^2$ to the $(4,2)$ walking mode is expected to arise. The relevant variables are defined in Table I.

parallel while the distance between them oscillates periodically at frequencies low relative to the bouncing frequency [17,18] (see Figs. 1 and 2).

Borghesi *et al.* [17] present a combined experimental and theoretical study of promenading pairs. Their experiments demonstrated that the mean interdrop distances are quantized and approximated by $\bar{x}_N = (N - \epsilon_0)\lambda_F$, where $\epsilon_0 \approx 0.4$ is an offset and N denotes the order of the promenade mode. We here adopt this notation, denoting promenaders bouncing in phase by $N = 1,2,3,\ldots$ and those bouncing out of phase by $N = 1.5,2.5,3.5,\ldots$. Borghesi *et al.* [17] reported that the mean translational speed v_N of a promenading pair in the Nth mode increases monotonically with N. The dependence of the promenading behavior on drop size and memory was not characterized. Their experiments also prompted some theoretical developments. Specifically, the authors show that the quantized distances $\bar{x}_N$ reported in experiments correspond to the minima of the wave interaction energy H_{int}, defined in terms of the amplitudes of the two wave fields generated by the walkers. They also show that the difference between the steady kinetic energy of two free walkers and the same pair bound in a promenade mode varies roughly linearly with H_{int} and interpret this as evidence that either may be used as a diagnostic to rationalize the emergence of the various promenade modes.

In Sec. II we will systematically characterize the behavior of promenading pairs as a function of memory. In Sec. III we will refine the stroboscopic model [22] and address its shortcomings in order to rationalize the observed behavior. Specifically, we demonstrate the importance of bouncing phase variations in stabilizing the promenading pairs.

II. EXPERIMENTS

A. Setup and methodology

The experiments were performed with the shaker system developed by Harris and Bush [23], which minimizes the lateral vibration provided to the fluid bath and ensures the spatial uniformity

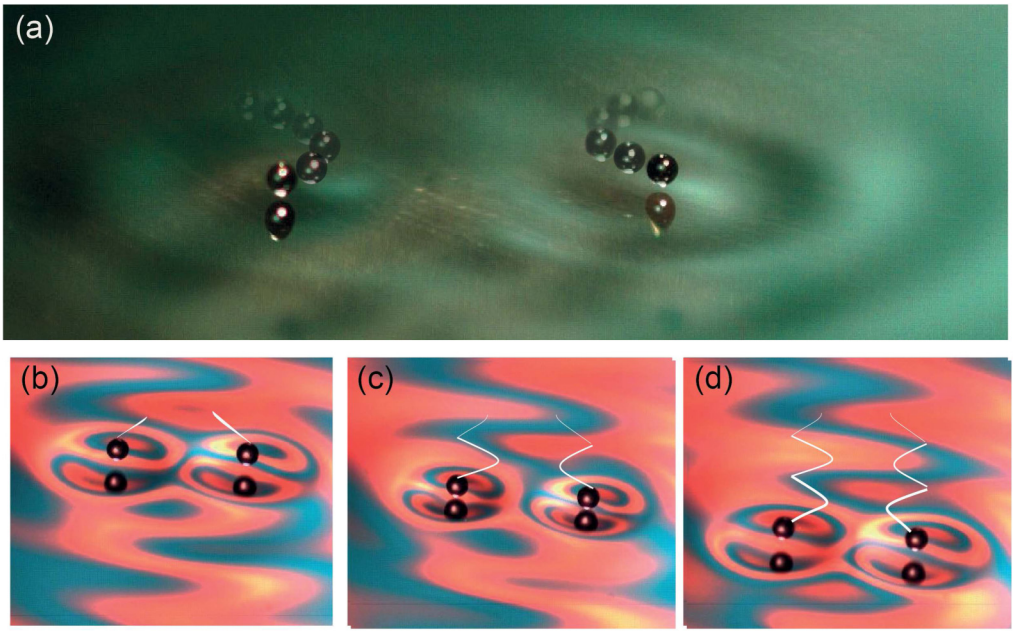

FIG. 2. (a) Strobed trajectories of an $N = 2$ stable promenading pair. (b)–(d) Oblique view of the strobed trajectory of an $N = 1$ promenade at different instants. The colors in the bath are due to the introduction of a colored striped transparent film between the lighting source and bath, which facilitates visualization of the surface deformations [20]. White lines indicate the trajectories of the droplets. See video 1 in [21].

of the Faraday threshold. We also employed a piezoelectric droplet-on-demand generator, which produces droplets of known and repeatable size [24]. Preliminary experiments indicated that air currents can significantly alter the trajectories of the promenaders [25]. We thus used a lid built from optically clear acrylic. Four rotating paddles passing through the lid (see Fig. 3) are used to trap the droplets in the holding pens prior to their simultaneous launch. The launcher consists of two channels positioned such that the distance between their exits matches the average distance $\overline{x}_N$ characteristic of the desired promenade mode, as was approximated by the empirical formula provided by Borghesi *et al.* [17]. A different launcher was constructed for each of the promenade modes N.

The fluid used in all experiments was silicone oil of kinematic viscosity $\nu = 20$ cSt, density $\rho = 949$ kg/m^3, and surface tension $\sigma = 20.6 \times 10^{-3}$ N/m. The trajectories were recorded from above with an Allied Vision Manta G-12 camera at 30 frames/s. The camera captured images of 964×964 pixels, corresponding to a resolution of 7.25 pixels/mm. The resulting error in the horizontal position of the droplet is ± 0.14 mm. The depth of the fluid bath was 6 mm, the diameter of the vessel 15.7 cm, and the forcing frequency $f = 80$ Hz. Note that a walker may bounce in different vertical modes [6,19,26,27], depending on its size and the vibrational forcing γ/γ_F [Fig. 1(e)]. Different bouncing and walking states are denoted by $(i, j)^k$, where i/f represents the period of the bouncing mode, during which the droplet contacts the surface j times. The integer superscript k increases with the state's mean mechanical energy in the case of multiple (i, j) bouncing states [19,26,27]. The parameter regime considered here is indicated in Fig. 1(e). Specifically, we restrict our attention to droplets of radius $R = 0.38 \pm 0.01$ mm and consider only two bouncing modes: the resonant walking mode $(2,1)^2$ and its period doubled $(4,2)$ mode.

The protocol used in the experiments is shown in Figs. 3(d)–3(f). The fluid bath was set into vibration and γ_F measured every 45 min in order to keep track of the memory γ/γ_F. Two droplets of identical size were created using the droplet generator [24]. The drop radii R were checked by recording their free walking speed u_0 and comparing with the known dependence [19] of speed on R.

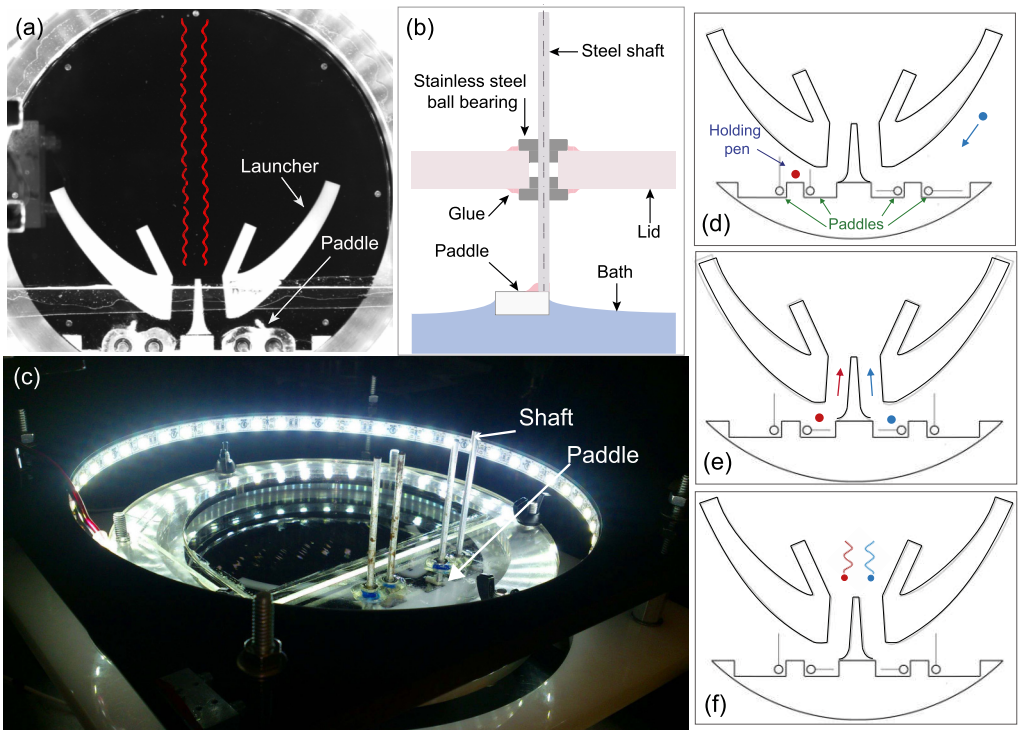

FIG. 3. (a) Top view of the lid, paddles, and launcher used to generate the $N = 2$ promenade mode. The red curves indicate the trajectory of each of the droplets. (b) Schematic of one of the rotating paddles. (c) Oblique view of the apparatus. (d)–(f) Protocol followed to generate the promenading pairs: (d) drop trapping, (e) release of the droplets from the holding pens, and (f) emergence of the desired promenading pair.

Specifically, we kept only the drops with speeds between 8.2 and 8.6 mm/s for $\gamma/\gamma_F = 0.9 \pm 0.002$, corresponding to drops of radius $R = 0.38 \pm 0.01$ mm. Once the droplet size was deduced, γ/γ_F was set to the desired value and the droplets were trapped in the holding pens with the paddles [Fig. 3(b)]. Using a strobe light, the relative bouncing phase of the trapped drops was deduced. If it was as desired, the downstream gates were opened and the promenading pair released from the launcher. If not, the phase of one of the drops was altered by perturbing it with one of the paddles prior to release. After recording one promenade, the memory γ/γ_F was increased and the droplets were trapped again in order to generate a new promenading pair.

B. Results

Stable promenaders for various N at a fixed value of memory are shown in Fig. 4. The duration of the promenades was limited by the size of the vessel; consequently, we were obliged to define a stable promenade as one that reached the opposite side of the vessel while maintaining the initial average distance between drops (i.e., the same N). According to this criterion, $N = 3$ and $N = 3.5$ were always unstable for droplets of radius $R = 0.38$ mm. However, decreasing the drop size increased the stability of the promenaders; for example, we were able to generate stable $N = 3$ modes with drops of radius $R = 0.35$ mm [Fig. 4(e)]. We note that with smaller droplets forced just above the walking threshold, it is possible to find stable promenaders with $N > 3.5$ [28].

The stability of the various promenading states with $R = 0.38$ mm is summarized in Fig. 5. For each N, we report a critical memory above which the droplets escape their partner and diverge. Evidently, promenaders with larger N become unstable at lower memories [see Fig. 5(a)]. This observation is consistent with the interaction force, specifically, the wave force due to

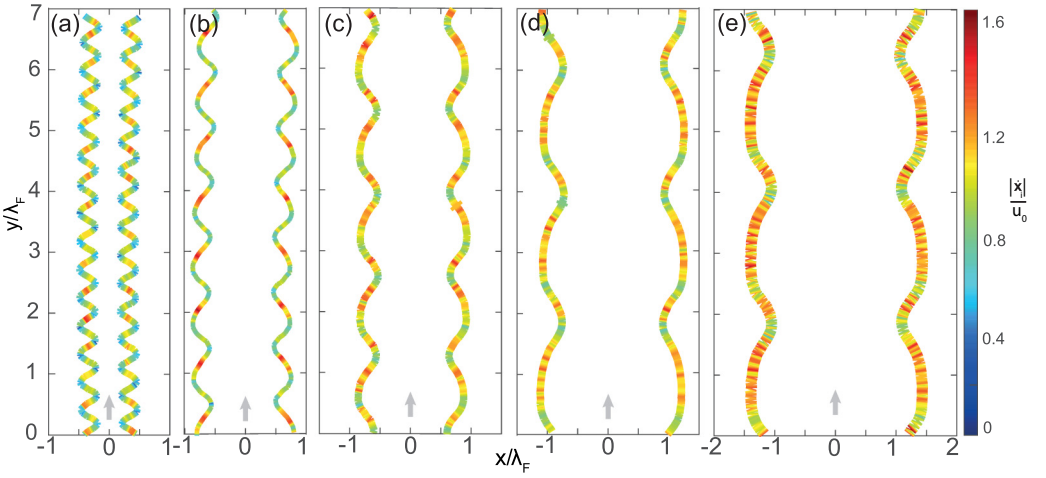

FIG. 4. Different stable promenading trajectories found in experiments at $\gamma/\gamma_F = 0.85 \pm 0.01$: (a) $N = 1$, (b) $N = 1.5$, (c) $N = 2$, (d) $N = 2.5$, and (e) $N = 3$. Trajectories are colored according to instantaneous speed $|\dot{\boldsymbol{x}}_i|$, nondimensionalized by the free walking speed u_0. All the promenaders were generated with a drop size of $R = 0.38$ mm, except the $N = 3$ mode, for which $R = 0.35$ mm.

the presence of the companion droplet, decreasing with interdroplet distance x_N. The smaller promenading modes $N = 1$ and $N = 1.5$ remained stable until relatively high memories $\gamma/\gamma_F = 0.99$. These modes were found to be extremely robust, even to reflection off the border of the vessel.

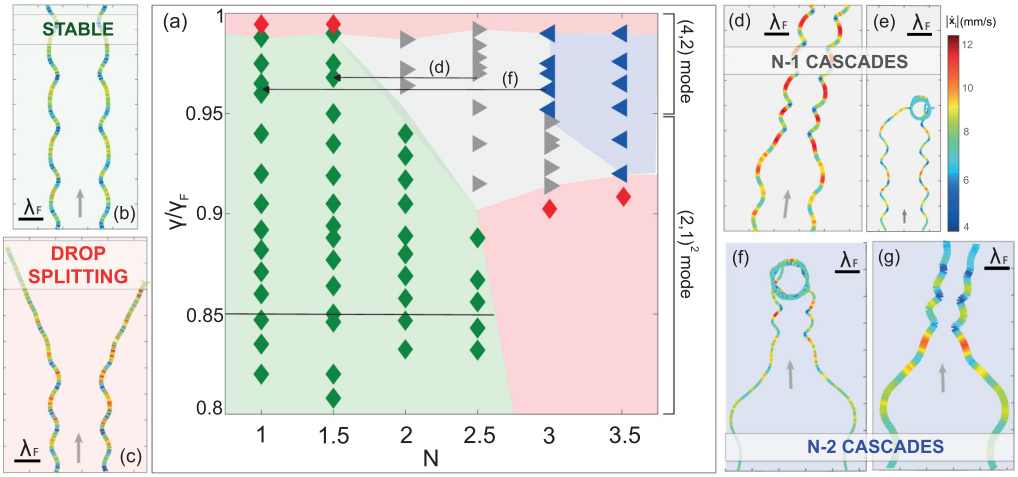

FIG. 5. (a) Observed stability of the promenading pairs as a function of the forcing acceleration γ/γ_F for drops of radius $R = 0.38$ mm. Green indicates stable promenaders. Red denotes drop splitting, with the data points indicating values of γ/γ_F above which the trajectories diverge for $N = 1$ and 1.5 and below which trajectories diverge for $N = 3$ and 3.5. Gray and blue denote consecutive and nonconsecutive cascades, respectively. The horizontal line at $\gamma/\gamma_F = 0.85$ indicates the parameter regime explored in Fig. 4. (b)–(g) Classification of the different observed behaviors. Arrows indicate the sense of motion. (b) Stable $N = 2.5$ promenade. (c) $N = 2.5$ promenade splitting. (d) Cascade from $N = 2.5$ to $N = 1.5$. (e) Cascade from an $N = 2$ promenade to an $N = 1$ orbit. (f) Cascade from an $N = 3.5$ promenade to an $N = 1.5$ orbit. (g) Cascade from the $N = 3$ to the $N = 1$ promenade mode, accompanied by a shift in direction. Trajectories are colored according to speed.

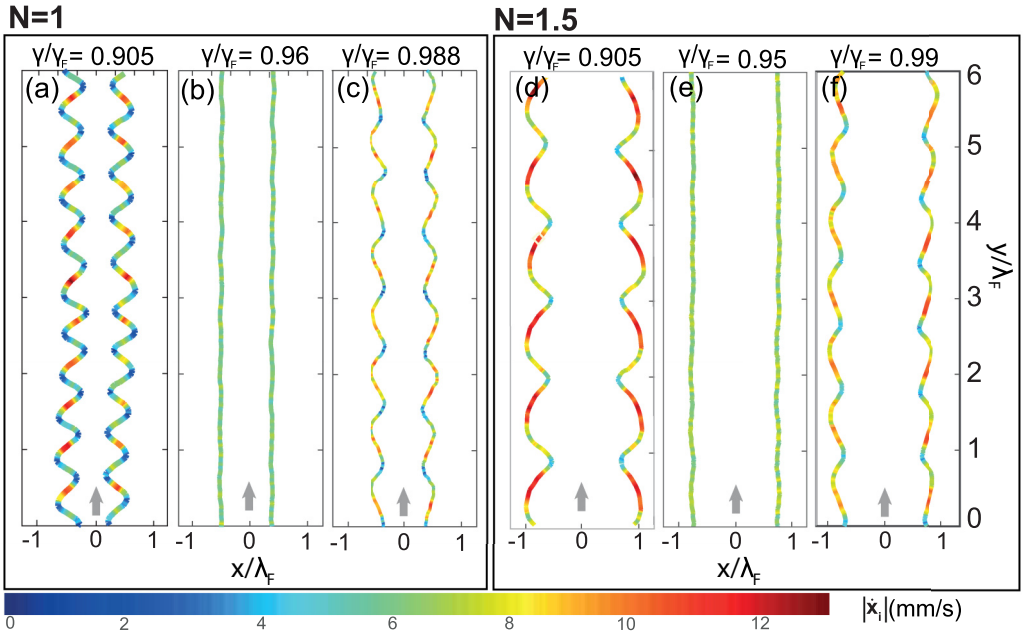

FIG. 6. Promenading trajectories for different values of γ/γ_F, colored according to the instantaneous drop speed: (a)–(c) $N = 1$ and (d)–(f) $N = 1.5$. Arrows indicate the sense of motion. Trajectories are shown (a) and (d) in the $(2,1)^2$ walking mode, (b) and (e) just after the transition to the (4,2) walking mode, and (c) and (f) that arise following the onset of chaos in the vertical dynamics.

The form of the promenading trajectories was also seen to depend on memory. Observed promenading trajectory modes $N = 1$ and $N = 1.5$ for different values of γ/γ_F are provided in Fig. 6. For memories above $\gamma/\gamma_F = 0.95$, a qualitative change in the trajectories was observed, in that the amplitude of the oscillations decreases dramatically. Notably, this critical memory value corresponds to that at which the vertical dynamics of single droplets exhibits a transition from the $(2,1)^2$ to the (4,2) walking mode [Fig. 1(e)], indicating the importance of vertical dynamics in the promenading pairs. Finally, we note that promenaders arise even after the onset of chaos in the vertical dynamics [Figs. 6(c) and 6(f)].

Video 2 in [21] reveals the marked difference in the vertical dynamics of the $N = 1$ promenade mode bouncing in the $(2,1)^2$ and (4,2) modes. In the $(2,1)^2$ mode, droplets hit the bath at precisely the same instant for integer values of N or apart by $T_F/2$ for half-integer values. However, consecutive bounces of $\sim 1.08T_F$ and $\sim 0.92T_F$ arise in the (4,2) mode. In order to maintain stability in the (4,2) bouncing mode, the droplets evidently adjust their relative phase, no longer being purely in phase or out of phase.

For the remainder of the paper, we adopt the convention that promenaders translate in the y direction and oscillate in the x direction. As shown in Figs. 7(a)–7(c), the average distance between droplets $\overline{x}_N \equiv \frac{1}{T_N}\int_0^{T_N} |\boldsymbol{x}_1(t) - \boldsymbol{x}_2(t)|dt$, their mean speed $u_N \equiv \frac{1}{T_N}\int_0^{T_N} |\dot{\boldsymbol{x}}(t)|dt$, and the period of oscillation T_N all increase with N for constant memory, where $\boldsymbol{x}_i$ is the horizontal position of drop i ($i = 1,2$). Note that the mean translational speeds $v_N \equiv \frac{1}{T_N}\int_0^{T_N} \dot{\boldsymbol{x}}_i(t) \cdot \hat{\boldsymbol{y}}dt$ are always lower than the corresponding free walking speed [Fig. 7(d)]. This is in accord with the observations of Borghesi *et al.* [17], who interpreted this observation as evidence of an effective binding energy between walkers. The periodic nature of the velocities is also evident in Figs. 4 and 6. While $\overline{x}_N$ [Fig. 9(a)] and T_N (not shown) depend only weakly on γ/γ_F, v_N depends strongly on memory, as is evident in Fig. 7(d). Figures 7(e) and 7(f) show u_N and v_N for the promenades $N = 1$ and $N = 1.5$. The

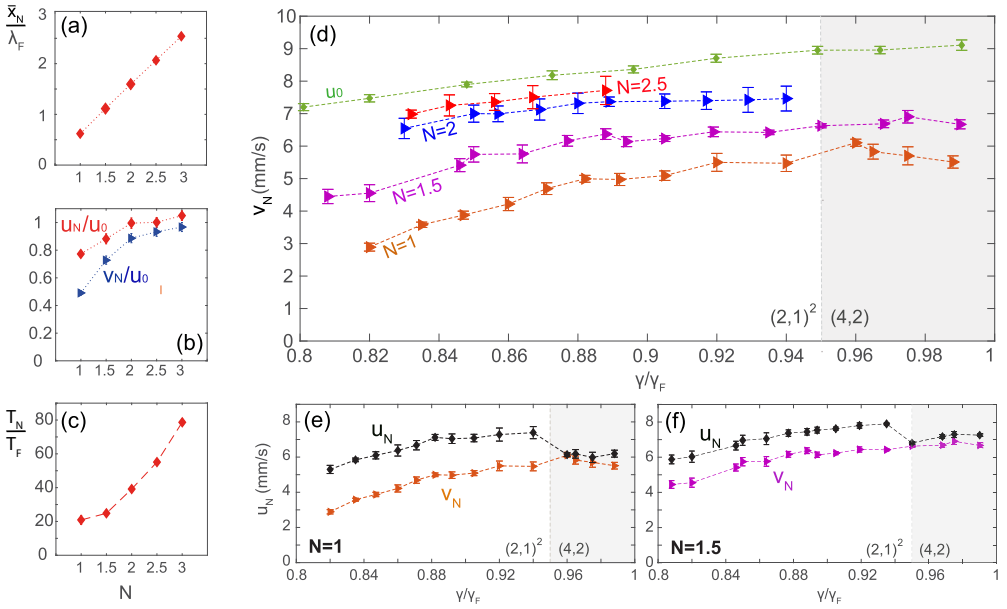

FIG. 7. Dependence of various promenade characteristics on the forcing acceleration γ/γ_F and mode N: (a)–(c) dependence on N for $\gamma/\gamma_F = 0.85 \pm 0.01$ and (d)–(f) dependence on γ/γ_F for the indicated values of N. (a) Mean interdrop distance $\overline{x}_N/\lambda_F$. (b) Pair speed. Here u_N denotes the mean total speed, v_N the mean translational speed, and u_0 the free walking speed. (c) Period of oscillation T_N/T_F. (d) Dependence of the mean translational speed v_N on γ/γ_F for different promenade modes $N = 1$ through $N = 2.5$. Note that v_N increases monotonically with increasing N. The shaded regions indicate droplets in the (4,2) vertical mode and the unshaded regions indicate the $(2,1)^2$ mode. Data for each promenade mode are reported until the critical memory at which it becomes unstable. Average drop speed u_N and mean translational speed v_N as a function of γ/γ_F for modes (e) $N = 1$ and (f) $N = 1.5$.

change in behavior of u_N at high memories is particularly evident, characterized by a diminution of the oscillation amplitudes of the interdroplet distance [Figs. 6(b) and 6(e)], and arises as a consequence of the transition in the bouncing mode from $(2,1)^2$ to (4,2).

For large γ/γ_F and for promenade modes initialized with $N > 1.5$, after a few oscillations, the initial promenade typically switched to a lower N promenade mode or alternatively to a lower N orbiting pair. We refer to these transitions as the "promenade cascades," examples of which are shown in Figs. 5(d)–5(g). The larger the value of N, the lower the memory required to initiate the cascades, as is evident in Fig. 5(a). During the cascades, the relative phase of the droplets was maintained. Several different transitions were found: At memories close to the onset of cascades, the large N mode typically decreased its order by one, changing to the $N - 1$ mode [Fig. 5(d)]. Following the transition, the new promenading pair can either maintain the initial direction or veer off its original path [see Fig. 5(g)]. At higher memory, a direct transition may arise to a lower $(N - 2)$ promenade mode or to orbital states.

III. THEORETICAL MODELING AND RESULTS

A. Stroboscopic model with impact phase adaptation

Consider two identical droplets of mass m and radius R, in the presence of a gravitational acceleration g promenading on the surface of a vertically vibrating bath of the same fluid, of surface tension σ, density ρ, and kinematic viscosity ν. The droplet's horizontal positions are denoted by

TABLE I. Variables and parameters appearing in the stroboscopic trajectory equation (1). Particular values for our experiments and simulations are: $R = 0.38$ mm, $\nu = 20$ cSt, $\rho = 949\,\mathrm{kg/m^3}$, $\sigma = 20.6 \times 10^{-3}$ N/m, $f = 80$ Hz, $T_F = 0.025$ s, $T_d = 0.0182$ s, $k_F = 1.32\ \mathrm{mm^{-1}}$, $\lambda_F = 4.75$ mm, $m = 2.18 \times 10^{-4}$ g, $D = 3.12 \times 10^{-3}$ g/s and $A = 0.0149$ mm.

Variable	Definition
$\boldsymbol{x}_i(t)$	Horizontal position of drop i, $(i = 1,2)$
m, R, ρ, σ	Drop mass, radius, density, surface tension
g	Gravitational acceleration
γ, γ_F, f	Forcing acceleration, Faraday threshold and frequency
$k_F, \lambda_F, T_F = 2/f$	Faraday wave number, wavelength, and period
T_d	Characteristic decay time of waves without forcing
$T_M = T_d/(1 - \gamma/\gamma_F)$	Memory time
$(\nu_e), \nu$	(Effective [19]) kinematic viscosity
μ_a, ρ_a	Air dynamic viscosity and density
$\varsigma = \pm 1$	Relative phase of the droplets (+ denotes in-phase)
$D = 0.33mg\sqrt{\frac{\rho R}{\sigma}} + 6\pi\mu_a R(1 + \frac{\rho_a g R}{12\mu_a f})$	Time-averaged drag coefficient [19]
$A = \frac{\sqrt{8\pi\nu_e T_F}}{3}\frac{(k_F R)^3}{3B_w^{-1}+1}$, $B_w = \frac{\rho g}{k_F^2\sigma}$	Wave amplitude [19], Bond number
$\Phi, \mathcal{S}$	Impact phase and its sine

$\boldsymbol{x}_1(t)$ and $\boldsymbol{x}_2(t)$, respectively. As the droplets are assumed to be in resonance with the bath, bouncing in the (2,1) mode, they can only bounce in phase ($\varsigma = 1$) or out of phase ($\varsigma = -1$). Each drop is propelled by a wave force proportional to the local slope of the wave field and resisted by drag induced during flight and impact [19]. Averaging the horizontal force on each droplet over the bouncing period yields the trajectory equation

$$m\ddot{\boldsymbol{x}}_i + D\dot{\boldsymbol{x}}_i = -mg\mathcal{S}(\tilde{h}_i(\boldsymbol{x}_i,t))\nabla h_i(\boldsymbol{x}_i,t) \tag{1}$$

for $i = 1$ and 2, where D is the time-averaged drag coefficient, h_i denotes the total wave field, $\tilde{h}_i$ is the wave field generated by the companion droplet, and $\mathcal{S}(\tilde{h}_i) = \sin[\Phi(\tilde{h}_i)]$ is the sine of the droplet's impact phase Φ, which depends explicitly on $\tilde{h}_i$. The remaining model parameters are defined in Table I.

We note that the phase function $\mathcal{S}(\tilde{h}_i)$ depends not on the total wave amplitude h but rather on the amplitude of the wave generated by the neighboring walker $\tilde{h}$. It has been shown that single rectilinear walkers may be adequately described by a stroboscopic trajectory equation [22] that assumes constant phase $\mathcal{S}$. The promenading path of either drop may be viewed as a perturbation from its rectilinear walking state, prompted by its partner. The perturbation induced by the neighboring walker thus enters in two places: the wave height h_i and the phase function $\mathcal{S}(\tilde{h}_i)$ in Eq. (1).

The stroboscopic model of Oza *et al.* [22] is based on the assumption that the walker is in resonance with the bath, so that the motion can be averaged over the bouncing period, the vertical dynamics described by Moláček and Bush [19] thereby being effectively eliminated from consideration. The impact phase Φ is defined by

$$\sin\Phi = \frac{1}{(mgT_F)^2}\left(\int_0^{T_F} F(t)\sin(\pi f t)dt\right)\left(\int_0^{T_F} F(t)\cos(\pi f t)dt\right), \tag{2}$$

where $F(t)$ is the vertical reaction force on the drop [27]. Calculation of Φ thus requires knowledge of the time dependence of the reaction force during contact, which may be obtained by solving for the vertical dynamics of the drop [27]. In order to rationalize the observed behavior of promenading pairs, a necessary refinement of the stroboscopic model [22] is the inclusion of a wave-amplitude-dependent impact phase. Including the dependence of impact phase on wave amplitude was previously shown to be necessary to rationalize the stability of orbiting pairs [15].

A derivation of the evolution of the wave field generated by one droplet walking on the surface of a vibrating bath $h_i(\boldsymbol{x},t)$ is provided elsewhere [19]. The total wave field felt by the first droplet may be obtained by superposition of the wave fields generated by each droplet impact:

$$h_1(\boldsymbol{x},t) = \frac{A}{T_F}\int_{-\infty}^{t}[J_0(k_F|\boldsymbol{x}-\boldsymbol{x}_1(s)|) + \varsigma J_0(k_F|\boldsymbol{x}-\boldsymbol{x}_2(s)|)]e^{-(t-s)/T_M}ds, \tag{3}$$

where A denotes the wave amplitude, J_0 denotes the Bessel function of the first kind, and the wave number has been approximated by the Faraday wave number k_F, as is related to the driving frequency f by the standard water-wave dispersion relation. The wave field felt by the second droplet may be obtained by interchanging $1 \leftrightarrow 2$ in the above expression. We note that $\varsigma = \pm 1$ accounts for the relative phase of the droplets. While spatial damping of the wave field has been shown to be significant for orbiting pairs [15], we here neglect it for the sake of simplicity. This simplification may be justified on the grounds that orbiting pairs execute periodic or quasiperiodic trajectories and remain in confined regions of space, thus continuously reenforcing their self-generated wave field. Conversely, promenaders move into previously unexplored regions, so one expects spatial damping to have a relatively small effect. Indeed, the spatial damping term $e^{-\alpha r^2/(t+T_F)}$ used previously [15] may be approximated as $e^{-\alpha v_N^2 t}$ for promenaders, which is subdominant to the exponential factor e^{-t/T_M} for the characteristic parameter values [15] in our experiments: $\alpha \sim 4\times 10^{-4}$ s/mm^2, $v_N \sim 10$ mm/s, and $\gamma/\gamma_F \leqslant 0.95$.

Introduction of the dimensionless variables $\hat{\boldsymbol{x}}_i = k_F\boldsymbol{x}_i$ and $\hat{t} = t/T_M$ into Eqs. (1) and (3) yields the dimensionless trajectory equation

$$\begin{aligned}
\kappa\hat{\boldsymbol{x}}_i'' + \hat{\boldsymbol{x}}_i' &= -\beta\mathcal{S}(\tilde{h}_i(\hat{\boldsymbol{x}}_i,\hat{t}))\nabla h_i(\hat{\boldsymbol{x}}_i,\hat{t}),\\
h_1(\hat{\boldsymbol{x}},\hat{t}) &= \frac{T_M}{T_F}\int_{-\infty}^{\hat{t}}[J_0(|\hat{\boldsymbol{x}}-\hat{\boldsymbol{x}}_1(\hat{s})|) + \varsigma J_0(|\hat{\boldsymbol{x}}-\hat{\boldsymbol{x}}_2(\hat{s})|)]e^{-(\hat{t}-\hat{s})}d\hat{s},\\
\tilde{h}_1(\hat{\boldsymbol{x}},\hat{t}) &= \frac{\varsigma T_M}{T_F}\int_{-\infty}^{\hat{t}}J_0(|\hat{\boldsymbol{x}}-\hat{\boldsymbol{x}}_2(\hat{s})|)e^{-(\hat{t}-\hat{s})}d\hat{s},
\end{aligned} \tag{4}$$

where $\kappa = m/DT_M$ and $\beta = mgAk_F^2T_M/D$ are the dimensionless mass and memory force coefficients, respectively, primes denote differentiation with respect to $\hat{t}$, and the amplitudes h_2 and $\tilde{h}_2$ are defined by replacing $1 \leftrightarrow 2$. For the sake of clarity, we henceforth remove all carets.

We seek solutions in which two droplets walk in parallel straight lines characterized by the interdrop distance x_N and the translational speed v_N of the pair's center of mass. The pair is assumed to walk parallel to the y axis, so trajectories take the form $\boldsymbol{x}_1(t) = (-x_N/2, v_N t)$ and $\boldsymbol{x}_2(t) = (x_N/2, v_N t)$. Substituting this form into Eq. (4) yields a system of two algebraic equations

$$\begin{aligned}
0 &= \int_0^\infty \frac{J_1\left(\sqrt{x_N^2+(v_N z)^2}\right)}{\sqrt{x_N^2+(v_N z)^2}}e^{-z}dz,\\
v_N &= \frac{\beta T_M}{T_F}\mathcal{S}\int_0^\infty\left(J_1(v_N z) + \varsigma\frac{J_1\left(\sqrt{x_N^2+(v_N z)^2}\right)}{\sqrt{x_N^2+(v_N z)^2}}v_N z\right)e^{-z}dz.
\end{aligned} \tag{5}$$

Given $\mathcal{S} = \sin\Phi$, these equations may be solved for x_N and v_N. Here, following the procedure introduced by Oza *et al.* [15], we use the experimental translational speeds v_N as input and solve for $\mathcal{S}$ and x_N as functions of γ/γ_F and N [Fig. 8(b)]. Doing so reveals that the impact phase decreases with forcing acceleration and increases with the promenade mode N. These trends are consistent with those reported for orbiting pairs of droplets [15], where the impact phases were calculated using the experimental orbital speed.

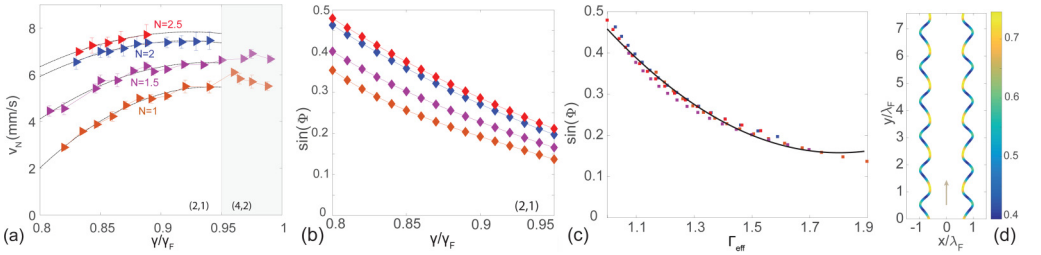

FIG. 8. Impact phase adaptation. (a) Observed translational velocities used in the base state algebraic equations (5). (b) Impact phases $\mathcal{S} = \sin\Phi$ provided by the base state equation (5), as a function of the promenade mode N and memory γ/γ_F. (c) Best-fit curve for the phase dependence indicated in (b), $\sin\Phi = p_3\Gamma_{\text{eff}}^2 + p_2\Gamma_{\text{eff}} + p_1$, as a function of the effective forcing $\Gamma_{\text{eff}} = \gamma/\gamma_F - p_4\tilde{h}$. The parameter values are $p_1 = 0.466$, $p_2 = -1.679$, $p_3 = 1.6705$, and $p_4 = 0.251$. (d) Simulation of an $N = 2$ promenade mode at $\gamma/\gamma_F = 0.84$, with the time evolution of the impact phase $\mathcal{S}(t)$ indicated in the color bar.

Once the mean impact phase of the promenaders has been determined, we deduce a semiempirical model for the dependence of the phase on the memory and the amplitude of the wave generated by the neighboring walker

$$\mathcal{S} = p_3\Gamma_{\text{eff}}^2 + p_2\Gamma_{\text{eff}} + p_1, \tag{6}$$

where $\Gamma_{\text{eff}} = \gamma/\gamma_F - p_4\tilde{h}$. In order to determine the constants p_i, we use the least-squares method in MATLAB to perform a fitting of the averaged phases provided by Eq. (5), where $\tilde{h} = \tilde{h}_w \equiv \frac{T_M\mathcal{S}}{T_F}\int_0^\infty J_0(\sqrt{x_N^2 + (v_N z)^2})e^{-z}dz$ in Eq. (6) is computable once Eq. (5) has been solved. This procedure yields the curve of best fit presented in Fig. 8(c).

Now that the dependence of $\mathcal{S}(\Gamma_{\text{eff}})$ has been determined, it can be used in the stability analysis and simulations of the trajectory equation (4). We thus model a time-dependent bouncing phase: As the drops navigate the wave field, their impact phase changes. Figure 8(d) shows an example of the predicted phase evolution for an $N = 2$ promenade mode.

B. Promenading pairs: Linear stability and simulations

In order to assess the stability of parallel straight-line walkers, we first solve Eq. (5) for the base state distance x_N and translational speed v_N. We find that the distance between droplets x_N is quantized and comparable to the average distances observed experimentally [see Fig. 9(a)].

We then perform a linear stability analysis of two parallel straight-line walkers $\boldsymbol{x}_1(t) = (-x_N/2, v_N t)$ and $\boldsymbol{x}_2(t) = (x_N/2, v_N t)$. We define new variables, the pair's center of mass $\boldsymbol{x}_c(t)$, the interdrop half-distance $r(t)$, and the angle $\theta(t)$ between the line connecting the walkers and the x axis,

$$\boldsymbol{x}_c(t) = \frac{1}{2}[\boldsymbol{x}_1(t) + \boldsymbol{x}_2(t)], \quad r(t)\begin{pmatrix}\cos\theta(t)\\ \sin\theta(t)\end{pmatrix} = \frac{1}{2}[\boldsymbol{x}_2(t) - \boldsymbol{x}_1(t)]. \tag{7}$$

In terms of the new variables, the base state assumes the form $\boldsymbol{x}_c(t) = (0, v_N t)$, $r(t) = x_N/2$, and $\theta(t) = 0$. As detailed in the Appendix, we linearize the trajectory equation (4) around this base state. We find that the Laplace transforms of the perturbations to the base state $X_c(s) = \mathcal{L}[\tilde{x}_c(t)]$, $Y_c(s) = \mathcal{L}[\tilde{y}_c(t)]$, $R(s) = \mathcal{L}[\tilde{r}(t)]$, and $\Theta(s) = \mathcal{L}[\tilde{\theta}(t)]$ satisfy an algebraic equation of

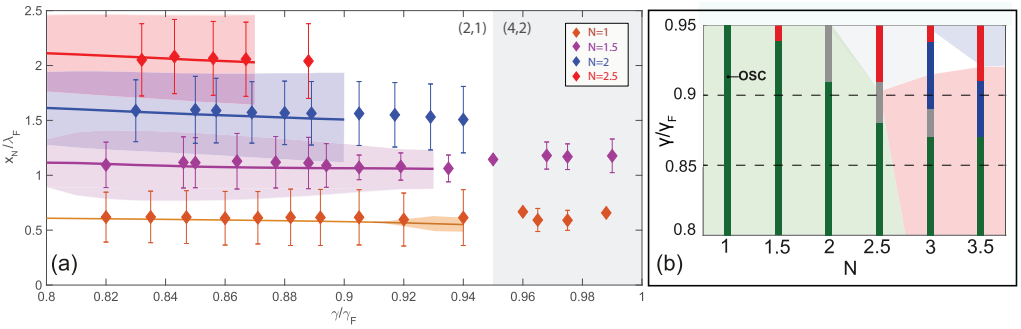

FIG. 9. Comparison between theory and experiment for a drop of radius $R = 0.38$ mm. (a) Data showing the dependence on γ/γ_F of the dimensionless average distance $\overline{x}_N/\lambda_F$ and amplitude of oscillation (indicated by error bars) for different promenade modes N colored according to the legend. Solid lines indicate results of the numerical simulation of Eq. (4) with phase adaptation consistent with Eq. (6). Shaded regions indicate maximum and minimum computed separation distance. (b) Stability characteristics predicted by the variable-phase stroboscopic model (vertical bars), color coded according to the color scheme used in Fig. 5(a). The background is shaded according to experimental observations. The predicted onset of transverse oscillations is indicated for the $N = 1$ mode. Red lines indicate drop trajectories crossing, owing to shortcomings in modeling the wave height near the droplet.

the form

$$\begin{pmatrix} \boldsymbol{M}^{+}(s) & 0 \\ 0 & \boldsymbol{M}^{-}(s) \end{pmatrix} \begin{pmatrix} R(s) \\ Y_c(s) \\ X_c(s) \\ (x_N/2)\Theta(s) \end{pmatrix} = \tilde{\boldsymbol{c}}, \tag{8}$$

where the elements of the 2×2 matrices $\boldsymbol{M}^{\pm}(s)$ and vector $\tilde{\boldsymbol{c}}$ are provided in the Appendix. The problem of finding the eigenvalues of the linearized equation is equivalent [29] to finding the poles s^* of $X_c(s)$, $Y_c(s)$, $R(s)$, and $\Theta(s)$, or the zeros of $\det \boldsymbol{M}^{\pm}(s)$. Specifically, if all of the poles lie in the left-half complex plane $\mathrm{Re}(s^*) < 0$, the parallel straight-line solution will be linearly stable. If any of the poles lie in the right-half complex plane $\mathrm{Re}(s^*) > 0$, the solution will be linearly unstable. We note that $\det \boldsymbol{M}^{-}(s)$ has a trivial double root at $s = 0$ and $\det \boldsymbol{M}^{+}(s)$ has a trivial single root at $s = 0$, which together correspond to translational and rotational invariance of the base state. In order to locate the nontrivial roots numerically, we use the contour integration method developed by Delves and Lyness [30]. For the parameter values considered in our experiments, we find that $\det \boldsymbol{M}^{-}(s)$ has no roots in the right-half complex plane, indicating that the parallel straight-line walkers are stable to lateral and angular perturbations ($\tilde{x}_c$ and $\tilde{\theta}$, respectively). We thus focus our attention on the roots of $\det \boldsymbol{M}^{+}(s)$, which indicate instabilities in the interdrop distance r and the position of the pair's center of mass y_c.

We find that the base state goes unstable via a Hopf-type bifurcation in which a pair of eigenvalues crosses the imaginary axis as γ/γ_F is increased, thus giving rise to an oscillatory instability. Our results also reveal that phase adaptation shifts down the curve of the real part of the eigenvalues, the decrement increasing with γ/γ_F. Conversely, the imaginary part of the eigenvalues is largely unaffected. The same trends arose for all promenade modes N. Thus, phase adaptation is seen to stabilize the promenading walkers. With the exception of $N = 1$, for which parallel straight-line walking is linearly stable until $\gamma/\gamma_F = 0.918$, the linear stability analysis predicts complex unstable eigenvalues for $\gamma/\gamma_F \geqslant 0.8$, whose real part increases with the driving acceleration, but remains close to zero. These results suggest the possibility of finding stable oscillatory promenaders when the full trajectory equation is solved instead of its linearized approximation.

We thus proceed by solving Eq. (4) numerically, in order to deduce whether or not the nonlinear terms have a stabilizing effect. We use a fourth-order Adams-Bashforth method together with Simpson's integration rule [31], with a dimensionless time step $\Delta t = 2^{-6}$. We initialize simulations in the parallel straight-line walking state $\boldsymbol{x}_1(t) = (-x_N/2, v_N t)$ and $\boldsymbol{x}_2(t) = (x_N/2, v_N t)$ for $t < 0$. In agreement with the linear stability analysis, our simulations indicate that side-by-side parallel straight line walkers are stable for $N = 1$ for $\gamma/\gamma_F < 0.918$, above which the straight-line state destabilizes into the promenade mode. The promenading solutions arising for $N \geqslant 1$ exist over a range of γ/γ_F above 0.8. The stroboscopic model correctly captures the trends observed in experiments: Speeds u_N and v_N increase with both N and memory. The larger the N, the lower the memory at which the promenade mode destabilizes. The average distance and amplitudes of oscillation are also in adequate agreement with the experimental values, as is evident in Fig. 9(a). The observed stability characteristics and the corresponding numerical results are provided in Fig. 9(b). We find that, as suggested by the linear stability analysis, introduction of phase adaptation into the model contributes significantly to the stabilization of the promenading pairs. Indeed, promenaders are stable for a considerably larger range of γ/γ_F when phase adaptation is included in the model, as was also the case for orbiters [15]. In the absence of consideration of phase adaptation, the model predicts in-phase cascades that appear at a γ/γ_F value $\sim$10% lower than in experiments. Moreover, the model without phase adaptation fails to capture cascades for $N = 2.5$. Once again, the introduction of phase adaptation has substantially improved the comparison between theory and experiment. We note that in our theoretical analysis, we restricted our attention to $\gamma/\gamma_F \leqslant 0.95$. For larger values of forcing, the walker transitions to (4,2) or chaotic bouncing states [26] where the stroboscopic trajectory equation (4) is no longer expected to be valid.

While including the dependence of the impact phase on forcing acceleration and local wave height improves the comparison with experiments, the match in Fig. 9(b) is still imperfect. First, parallel straight-line walkers for $N = 1$ are predicted to be stable for $\gamma/\gamma_F < 0.918$, but were never observed experimentally. Second, our theory underpredicts the critical values of γ/γ_F at which the promenade modes become unstable, as shown in Fig. 9(a). We note that a similar trend was apparent in our assessment of the stability of orbiting pairs [15]. These failings of our theory are presumably due to shortcomings in the model of the wave field near the droplet. Finally, we do not expect the dynamics at high memory to be adequately described by the stroboscopic model due to the transition to more complicated bouncing states. Specifically, as indicated in Fig. 1(e), the experimental results of Wind-Willassen *et al.* [26] indicate that drops with vibration number $2\pi f/\sqrt{\sigma/\rho R^3} \approx 0.793$ transition to a (4,2) bouncing state at $\gamma/\gamma_F \approx 0.93$ and to a chaotic bouncing state for $\gamma/\gamma_F \approx 0.97$.

C. Interaction force between walkers

In an attempt to rationalize the cascade events, we consider the wave force acting on an individual droplet, defined in dimensionless variables as

$$\boldsymbol{F}_i(t) = -\beta \mathcal{S}(\tilde{h}_i(\boldsymbol{x}_i(t),t))\nabla h_i(\boldsymbol{x}_i(t),t). \tag{9}$$

Specifically, this represents the wave force that droplet i receives due to the wave field created by its previous bounces plus the wave field due to the presence of its companion promenader. We proceed by considering the x component of the wave force, which acts along the line connecting the two droplets.

Figure 10 shows that, when the droplets maintain a stable oscillatory promenade, the wave force forms a hysteresis loop: The instantaneous force depends not only on the drops' positions but on whether they are moving inward or outward, the force being larger when the drops are moving towards each other. As γ/γ_F is increased progressively, so too does the memory-induced hysteresis [Fig. 10(a)]. Additionally, computations show that for a fixed value of memory, the wave force due to the companion droplet becomes weaker as N is increased [Fig. 10(b)], which is consistent with the observation of larger promenaders splitting at lower values of the γ/γ_F and having higher translational velocity v_N. While the analytical model presented by Borghesi *et al.* [17] represents the

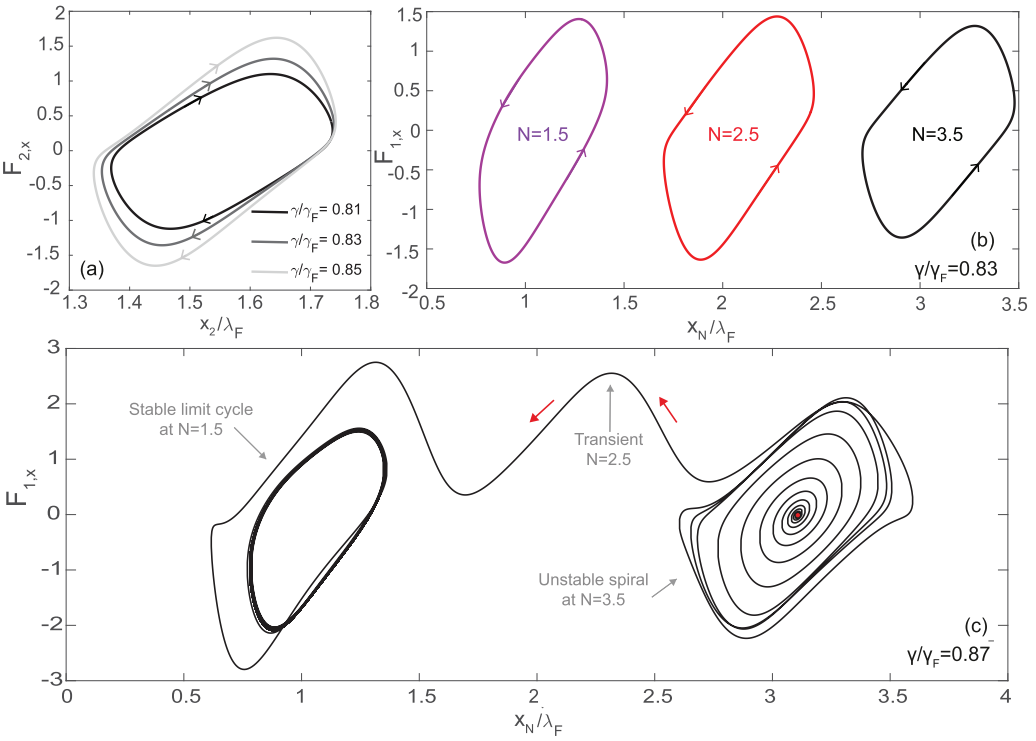

FIG. 10. (a) The x component of the force $\boldsymbol{F}_i(t)$, as defined by Eq. (9), exerted by the wave field on one of the $N = 3.5$ promenading droplets as a function of its position $x_2(t)$ at different values of the memory γ/γ_F. Note that the area inside the curves represents the work done by the x component of the wave force during one oscillation period of the promenader. (b) The x component of the wave force as a function of the interdroplet distance x_N for out-of-phase promenaders at $\gamma/\gamma_F = 0.83$. (c) Cascade from $N = 3.5$ to $N = 1.5$. The red dot represents the base state used in simulations.

force between promenaders as a linear spring, our findings highlight the shortcomings of doing so, particularly in the high memory limit.

For each $N \geqslant 2$, our model predicts a critical value of γ/γ_F at which a bifurcation arises: Promenading trajectories destabilize via an unstable spiral and transition to a stable promenade mode at lower N, which corresponds to the cascades [gray and blue in Fig. 9(b)]. An example of such a trajectory is shown in Fig. 10(c), which shows that the droplets transition from an $N = 3.5$ to an $N = 1.5$ promenade mode when the distance between droplets oscillates with amplitude $\sim\lambda_F$. Physically, a droplet bound in a stable promenading state lies roughly in the trough of the wave field created by its companion. For the cascades, the interaction force on the droplets is evidently sufficiently large to enable them to escape to a trough corresponding to a lower N value.

Figure 10(a) demonstrates that the horizontal wave force applied on a promenading droplet grows with γ/γ_F, as does the area enclosed by the force-displacement curve, which corresponds to the work done by the x component of the wave force. Attempts to rationalize the relative stability of the different promenade modes by calculating this work as a function of γ/γ_F were unsuccessful. Following Borghesi *et al.* [17], we define the binding energy of the bound state as $W_{\text{bind}} = W_p - 2W_w$, where W_p represents the work done by the wave force on a promenading pair and W_w the work done by the wave force on an identical free walker over the same time interval T_N, specifically,

$$W_p = \int_0^{T_N} [\boldsymbol{F}_1(t) \cdot \dot{\boldsymbol{x}}_1(t) + \boldsymbol{F}_2(t) \cdot \dot{\boldsymbol{x}}_2(t)]dt, \quad W_w = \int_0^{T_N} \boldsymbol{F}_1(t) \cdot \dot{\boldsymbol{x}}_1(t)dt. \tag{10}$$

Had there been a change in the relative magnitudes of the binding energies of the various promenading states with γ/γ_F, one would expect this to indicate a shift in their relative stability. However, we did not find such changes, suggesting that the smaller promenaders are the most stable regardless of the value of γ/γ_F.

While the binding energy of the promenading pairs, as defined in Eq. (10), provides a measure of the work done in confining the drop's horizontal motion, it fails to provide rationale for the stability of the various promenading states, specifically, the dependence of their relative stability on memory. The failings of this binding energy as a useful diagnostic of the relative stability of the promenading states arises because the dominant energies in the system are associated with the drop's vertical dynamics, as evidenced by the fact that the vertical drop velocities are roughly ten times higher than their horizontal counterparts. We thus conclude that the work done by the wave field in the horizontal direction is negligible relative to that associated with the accompanying modulation of the drop's vertical dynamics, which is not considered in the stroboscopic model. A more complete treatment of the energetics which incorporates bouncing phase variations is beyond the scope of the present work.

IV. CONCLUSION

We have extended the observations of Borghesi *et al.* [17] by characterizing the role of memory on the stability of promenading pairs of walking droplets. We observed that the larger the N, the lower the memory at which the promenade destabilization occurs. We also reported that at sufficiently high memory, the largest promenaders may spontaneously cascade to smaller bound states, either promenaders or orbiters. Finally, we observe that large $N > 3.5$ promenaders may be achieved for relatively small droplets.

We also found that small promenaders, $N = 1$ and $N = 1.5$, maintain stable oscillatory motion even at high memory, where they enter the (4,2) or a chaotic bouncing mode and continuously adapt their relative phase while maintaining a bound state. Our study provides evidence that the (4,2) bouncing mode has a stabilizing effect on the promenading pairs; specifically, once the pair enters the (4,2) mode, it remains stable until relatively high memory. Moreover, promenading pairs formed by relatively small drops maintain a stable interaction until higher memory, presumably because the transition to the (4,2) mode occurs at relatively low values of γ/γ_F [see Fig. 1(e)].

In order to rationalize our experimental findings, the dependence of impact phase on local wave amplitude had to be considered. We did so by adopting a semiempirical formula for $\Phi(\tilde{h})$ in the stroboscopic model (4). This phase adaptation was shown to have a stabilizing effect on promenade modes and so to improve substantially the match between theory and experiments. The promenading trajectories predicted by numerical simulations of the resulting variable-phase stroboscopic model correctly capture the main experimental features: The distance between droplets is quantized and in good agreement with experimental values, and translational velocities increase with N. The model also captures the promenade cascades, in which promenading pairs transition to smaller N or into circular orbits. However, promenaders at high memory in the (4,2) or chaotic bouncing modes could not be adequately captured, as the stroboscopic model assumes a resonant $(2,1)^2$ vertical bouncing mode. A general treatment of walker dynamics in which both spatial damping and phase adaptation are modeled is left for future work.

Borghesi *et al.* [17] limited their analytical work to the low memory limit, specifically, they consider only the influence of the last impact. While their numerical simulations incorporated the walkers' histories, their analytical model represented the interaction force as a linear spring: The force depended only on the instantaneous distance between droplets. Our study demonstrates the role that memory-induced hysteresis plays in modeling the promenaders at higher memories [Fig. 10(a)]. It has also highlighted the importance of vertical dynamics, specifically, bouncing-phase adaptation in stabilizing promenading pairs, a feature not previously considered [17,18].

This exploration of the promenade mode, in conjunction with the recent study of orbiting pairs [15], indicates that the role of variable impact phase is significant in the stabilization of bound states formed by droplet interactions. Phase-dependent bouncing is likewise expected to play a role in

stabilizing the circular orbits of single droplets, either in isolation [4,22,32] or in the presence of an external force [5,9,29,33–35]. Indeed, for walker motion both in a rotating frame and in the presence of a harmonic potential, wobbling circular orbits were far more prevalent in experiment [9,33] than was indicated by the linear stability theory developed from the stroboscopic model without phase adaptation [29,34]. Developing a more general description of the dependence of the phase on the wave amplitude and memory is left for future work. Finally, consideration of the energetics of the system may provide a new rationale for the relative stability of the promenade modes [17] and, more generally, for the emergence of bound states in multidroplet systems. An analysis of the energetics of single and multiple bouncer and walker systems is also left for future work.

ACKNOWLEDGMENTS

J.W.M.B. gratefully acknowledges support from the NSF through Grants No. CMMI-1333242 and No. DMS-1614043. A.U.O. acknowledges support from the NSF Mathematical Sciences Postdoctoral Fellowship, with the associated Grant No. DMS-1400934. We thank Giuseppe Pucci, Emmanuel Siéfert, and Miles Couchman for valuable assistance and discussion.

APPENDIX

We here assess the linear stability of the side-by-side walking state. To this end, we substitute the expressions $\boldsymbol{x}_1(t) = (-x_N/2, v_N t) + \tilde{\boldsymbol{x}}_1(t)H(t)$ and $\boldsymbol{x}_2(t) = (x_N/2, v_N t) + \tilde{\boldsymbol{x}}_2(t)H(t)$ into the trajectory equation (4) and retain terms at leading order in the perturbations $\tilde{\boldsymbol{x}}_i(t)$, where x_N and v_N are defined in Eq. (5) and $H(t)$ is the Heaviside function. To simplify the notation, we define the function $f(r,t) = \frac{T_M}{T_F} J_0(r)e^{-t}$ and the functions

$$f_0(z) = f\Big(\sqrt{x_N^2 + (v_N z)^2}, z\Big), \quad f_1(z) = \frac{f_r\Big(\sqrt{x_N^2 + (v_N z)^2}, z\Big)}{\sqrt{x_N^2 + (v_N z)^2}}, \quad f_2(z) = f_{rr}\Big(\sqrt{x_N^2 + (v_N z)^2}, z\Big),$$

$$g_1(z) = \frac{f_r(v_N z, z)}{v_N z}, \quad g_2(z) = f_{rr}(v_N z, z). \tag{A1}$$

We also use the fact that Eq. (5) can be written as

$$\begin{pmatrix} 0 \\ v_N \end{pmatrix} = -\beta \mathcal{S}(\tilde{h}_w) \int_0^\infty \left[g_1(z) \begin{pmatrix} 0 \\ v_N z \end{pmatrix} + \varsigma f_1(z) \begin{pmatrix} x_N \\ v_N z \end{pmatrix} \right] dz \tag{A2}$$

where $\tilde{h}_w = \varsigma \int_0^\infty f_0(z) dz$, and note that

$$\nabla \left(\frac{g(|\boldsymbol{x}|)}{|\boldsymbol{x}|} \boldsymbol{x} \right) = \frac{g(|\boldsymbol{x}|)}{|\boldsymbol{x}|} \boldsymbol{I} + \left(g'(|\boldsymbol{x}|) - \frac{g(|\boldsymbol{x}|)}{|\boldsymbol{x}|} \right) \frac{\boldsymbol{x}\boldsymbol{x}}{|\boldsymbol{x}|^2}, \tag{A3}$$

where $\boldsymbol{I}$ is the identity matrix. We obtain the linearized equation

$$\begin{aligned} \kappa \ddot{\tilde{\boldsymbol{x}}}_1 + \dot{\tilde{\boldsymbol{x}}}_1 = {} & \frac{\varsigma v_N \mathcal{S}'}{\mathcal{S}} \begin{pmatrix} 0 \\ 1 \end{pmatrix} \int_{-\infty}^t f_1(z) \begin{pmatrix} -x_N \\ v_N z \end{pmatrix} \cdot [\tilde{\boldsymbol{x}}_1(t) - \tilde{\boldsymbol{x}}_2(s)H(s)] ds \\ & - \beta \mathcal{S} \int_{-\infty}^t \begin{pmatrix} g_1(z) & 0 \\ 0 & g_2(z) \end{pmatrix} [\tilde{\boldsymbol{x}}_1(t) - \tilde{\boldsymbol{x}}_1(s)H(s)] ds \\ & - \varsigma \beta \mathcal{S} \int_{-\infty}^t f_1(z) [\tilde{\boldsymbol{x}}_1(t) - \tilde{\boldsymbol{x}}_2(s)H(s)] ds \\ & - \varsigma \beta \mathcal{S} \int_{-\infty}^t \frac{f_2(z) - f_1(z)}{x_N^2 + (v_N z)^2} \begin{pmatrix} x_N^2 & -x_N v_N z \\ -x_N v_N z & (v_N z)^2 \end{pmatrix} [\tilde{\boldsymbol{x}}_1(t) - \tilde{\boldsymbol{x}}_2(s)H(s)] ds, \end{aligned} \tag{A4}$$

where $z = t - s$, and both $\mathcal{S}$ and $\mathcal{S}' \equiv \partial\mathcal{S}/\partial\tilde{h}$ are evaluated at $\tilde{h}_w$. The analogous equation for $\tilde{\boldsymbol{x}}_2$ is obtained by interchanging $\tilde{\boldsymbol{x}}_1 \leftrightarrow \tilde{\boldsymbol{x}}_2$ and replacing $x_N \to -x_N$ in Eq. (A4). Taking the Laplace transform of both sides of Eq. (A4) and assuming that $\tilde{\boldsymbol{x}}_i(0) = 0$, we obtain

$$\begin{pmatrix} \boldsymbol{A}_-(s) & \boldsymbol{B}_-(s) \\ \boldsymbol{B}_+(s) & \boldsymbol{A}_+(s) \end{pmatrix} \begin{pmatrix} \boldsymbol{X}_1(s) \\ \boldsymbol{X}_2(s) \end{pmatrix} = \boldsymbol{c}, \tag{A5}$$

where $\boldsymbol{X}_i(s) = \mathcal{L}[\tilde{\boldsymbol{x}}_i(t)] \equiv \int_0^\infty \tilde{\boldsymbol{x}}_i(t) e^{-st} dt$ and $\boldsymbol{c} = \kappa \binom{\dot{x}_1(0)}{\dot{x}_2(0)}$. The 2×2 matrices $\boldsymbol{A}_\pm(s)$ and $\boldsymbol{B}_\pm(s)$ are defined as

$$\begin{aligned} \boldsymbol{A}_\pm(s) &= (\kappa s^2 + s)\boldsymbol{I} - \frac{\varsigma v_N \mathcal{S}'}{\mathcal{S}} \int_0^\infty f_1(z) \begin{pmatrix} 0 & 0 \\ \pm x_N & v_N z \end{pmatrix} dz - \beta\mathcal{S}\mathcal{L}_-\left[\begin{pmatrix} g_1(t) & 0 \\ 0 & g_2(t) \end{pmatrix}\right] \\ &\quad + \varsigma\beta\mathcal{S}\boldsymbol{I} \int_0^\infty f_1(z) dz + \varsigma\beta\mathcal{S} \int_0^\infty \frac{f_2(z) - f_1(z)}{x_N^2 + (v_N z)^2} \begin{pmatrix} x_N^2 & \pm x_N v_N z \\ \pm x_N v_N z & (v_N z)^2 \end{pmatrix} dz, \\ \boldsymbol{B}_\pm(s) &= \frac{\varsigma v_N \mathcal{S}'}{\mathcal{S}} \mathcal{L}\left[f_1(t) \begin{pmatrix} 0 & 0 \\ \pm x_N & v_N t \end{pmatrix}\right] - \varsigma\beta\mathcal{S}\boldsymbol{I}\mathcal{L}[f_1(t)] \\ &\quad - \varsigma\beta\mathcal{S}\mathcal{L}\left[\frac{f_2(t) - f_1(t)}{x_N^2 + (v_N t)^2} \begin{pmatrix} x_N^2 & \pm x_N v_N t \\ \pm x_N v_N t & (v_N t)^2 \end{pmatrix}\right], \end{aligned} \tag{A6}$$

where $\mathcal{L}_\pm[g(t)] \equiv \int_0^\infty g(t)(e^{-st} \pm 1) dt$.

To simplify Eq. (A5), we introduce the center-of-mass variables

$$\boldsymbol{x}_c(t) = \frac{1}{2}[\boldsymbol{x}_1(t) + \boldsymbol{x}_2(t)], \quad r(t) \begin{pmatrix} \cos\theta(t) \\ \sin\theta(t) \end{pmatrix} = \frac{1}{2}[\boldsymbol{x}_2(t) - \boldsymbol{x}_1(t)]. \tag{A7}$$

Perturbations around the base state are defined through the formulas $\boldsymbol{x}_c(t) = (0, v_N t) + \tilde{\boldsymbol{x}}_c(t)$, $r(t) = x_N/2 + \tilde{r}(t)$, and $\theta(t) = \tilde{\theta}(t)$ and are thus related to the perturbations $\tilde{\boldsymbol{x}}_i(t)$ by the equation $\binom{\tilde{\boldsymbol{x}}_1}{\tilde{\boldsymbol{x}}_2} = \boldsymbol{J}\boldsymbol{q}$, where

$$\boldsymbol{q}(t) = \begin{pmatrix} \tilde{r} \\ \tilde{y}_c \\ \tilde{x}_c \\ (x_N/2)\tilde{\theta} \end{pmatrix}, \quad \boldsymbol{J} = \begin{pmatrix} -\boldsymbol{Z} & \boldsymbol{Z} \\ \boldsymbol{I} & \boldsymbol{I} \end{pmatrix}, \quad \boldsymbol{Z} = \begin{pmatrix} 1 & 0 \\ 0 & -1 \end{pmatrix}. \tag{A8}$$

Defining $\boldsymbol{Q}(s) = \mathcal{L}[\boldsymbol{q}(t)]$ and $\tilde{\boldsymbol{c}} = \boldsymbol{J}^{-1}\boldsymbol{c}$, Eq. (A5) may be written as $\boldsymbol{M}(s)\boldsymbol{Q}(s) = \tilde{\boldsymbol{c}}$, where

$$\boldsymbol{M}(s) = \boldsymbol{J}^{-1} \begin{pmatrix} \boldsymbol{A}_-(s) & \boldsymbol{B}_-(s) \\ \boldsymbol{B}_+(s) & \boldsymbol{A}_+(s) \end{pmatrix} \boldsymbol{J} = \begin{pmatrix} \boldsymbol{A}_1 - \boldsymbol{B}_1 & \boldsymbol{A}_2 + \boldsymbol{B}_2 \\ \boldsymbol{A}_2 - \boldsymbol{B}_2 & \boldsymbol{A}_1 + \boldsymbol{B}_1 \end{pmatrix}, \tag{A9}$$

with $\boldsymbol{A}_1 = (\boldsymbol{A}_+ + \boldsymbol{Z}\boldsymbol{A}_-\boldsymbol{Z})/2$, $\boldsymbol{A}_2 = (\boldsymbol{A}_+ - \boldsymbol{Z}\boldsymbol{A}_-\boldsymbol{Z})/2$, $\boldsymbol{B}_1 = (\boldsymbol{B}_+\boldsymbol{Z} + \boldsymbol{Z}\boldsymbol{B}_-)/2$, and $\boldsymbol{B}_2 = (\boldsymbol{B}_+\boldsymbol{Z} - \boldsymbol{Z}\boldsymbol{B}_-)/2$. Since $\boldsymbol{A}_2 = \boldsymbol{B}_2 = 0$, $\boldsymbol{A}_1 = \boldsymbol{A}_+$, and

$$\begin{aligned} \boldsymbol{B}_1(s) &= \frac{\varsigma v_N \mathcal{S}'}{\mathcal{S}} \mathcal{L}\left[f_1(t) \begin{pmatrix} 0 & 0 \\ x_N & -v_N t \end{pmatrix}\right] - \varsigma\beta\mathcal{S}\boldsymbol{Z}\mathcal{L}[f_1(t)] \\ &\quad - \varsigma\beta\mathcal{S}\mathcal{L}\left[\frac{f_2(t) - f_1(t)}{x_N^2 + (v_N t)^2} \begin{pmatrix} x_N^2 & -x_N v_N t \\ x_N v_N t & -(v_N t)^2 \end{pmatrix}\right], \end{aligned} \tag{A10}$$

$\boldsymbol{M}(s)$ assumes the block diagonal form $\boldsymbol{M}(s) = \begin{pmatrix} \boldsymbol{M}^{+}(s) & 0 \\ 0 & \boldsymbol{M}^{-}(s) \end{pmatrix}$, where the 2×2 matrices $\boldsymbol{M}^{\pm}(s)$ have matrix elements

$$
\begin{aligned}
\boldsymbol{M}^{\pm}_{11} &= \kappa s^2 + s - \beta \mathcal{S} \mathcal{L}_{-}[g_1(t)] \pm \varsigma \beta \mathcal{S} \mathcal{L}_{\pm}\left[\frac{f_2(t) x_N^2 + f_1(t)(v_N t)^2}{x_N^2 + (v_N t)^2}\right], \\
\boldsymbol{M}^{\pm}_{12} &= \mp \varsigma \beta \mathcal{S} \mathcal{L}_{\mp}\left[\frac{f_2(t) - f_1(t)}{x_N^2 + (v_N t)^2} x_N v_N t\right], \\
\boldsymbol{M}^{\pm}_{21} &= \mp \frac{\varsigma v_N x_N \mathcal{S}'}{\mathcal{S}} \mathcal{L}_{\pm}[f_1(t)] \pm \varsigma \beta \mathcal{S} \mathcal{L}_{\pm}\left[\frac{f_2(t) - f_1(t)}{x_N^2 + (v_N t)^2} x_N v_N t\right], \\
\boldsymbol{M}^{\pm}_{22} &= \kappa s^2 + s - \beta \mathcal{S} \mathcal{L}_{-}[g_2(t)] \pm \frac{\varsigma v_N \mathcal{S}'}{\mathcal{S}} \mathcal{L}_{\mp}[f_1(t) v_N t] \mp \varsigma \beta \mathcal{S} \mathcal{L}_{\mp}\left[\frac{f_2(t)(v_N t)^2 + f_1(t) x_N^2}{x_N^2 + (v_N t)^2}\right].
\end{aligned}
\tag{A11}
$$

[1] J. Miles and D. Henderson, Parametrically forced surface waves, Annu. Rev. Fluid Mech. **22**, 143 (1990).

[2] J. Walker, Drops of liquid can be made to float on the liquid. What enables them to do so?, Sci. Am. **238**, 151 (1978).

[3] S. Protière, A. Boudaoud, and Y. Couder, Particle-wave association on a fluid interface, J. Fluid. Mech. **554**, 85 (2006).

[4] J. W. M. Bush, Pilot-wave hydrodynamics, Annu. Rev. Fluid Mech. **47**, 269 (2015).

[5] E. Fort, A. Eddi, J. Moukhtar, A. Boudaoud, and Y. Couder, Path-memory induced quantization of classical orbits, Proc. Natl. Acad. Sci. USA **107**, 17515 (2010).

[6] A. Eddi, E. Sultan, J. Moukhtar, E. Fort, M. Rossi, and Y. Couder, Information stored in Faraday waves: The origin of a path memory, J. Fluid Mech. **674**, 433 (2011).

[7] D. M. Harris, J. Moukhtar, E. Fort, Y. Couder, and J. W. M. Bush, Wavelike statistics from pilot-wave dynamics in a circular corral, Phys. Rev. E **88**, 011001(R) (2013).

[8] A. Eddi, E. Fort, F. Moisy, and Y. Couder, Unpredictable Tunneling of a Classical Wave-Particle Association, Phys. Rev. Lett. **102**, 240401 (2009).

[9] S. Perrard, M. Labousse, M. Miskin, E. Fort, and Y. Couder, Self-organization into quantized eigenstates of a classical wave-driven particle, Nat. Commun. **5**, 3219 (2014).

[10] Y. Couder and E. Fort, Probabilities and trajectories in a classical wave-particle duality, J. Phys. Conf. Ser. **361**, 012001 (2012).

[11] J. W. M. Bush, The new wave of pilot-wave theory, Phys. Today **68**(8), 47 (2015).

[12] S. I. Lieber, M. C. Hendershott, A. Pattanaporkratana, and J. E. Maclennan, Self-organization of bouncing oil drops: Two-dimensional lattices and spinning clusters, Phys. Rev. E **75**, 056308 (2007).

[13] A. Eddi, A. Decelle, E. Fort, and Y. Couder, Archimedean lattices in the bound states of wave interacting particles, Europhys. Lett. **87**, 56002 (2009).

[14] A. Eddi, A. Boudaoud, and Y. Couder, Oscillating instability in bouncing droplet crystals, Europhys. Lett. **94**, 20004 (2011).

[15] A. U. Oza, E. Siéfert, D. M. Harris, J. Moláček, and J. W. M. Bush, Orbiting pairs of walking droplets: Dynamics and stability, Phys. Rev. Fluids **2**, 053601 (2017).

[16] A. Eddi, D. Terwagne, E. Fort, and Y. Couder, Wave propelled ratchets and drifting rafts, Europhys. Lett. **82**, 44001 (2008).

[17] C. Borghesi, J. Moukhtar, M. Labousse, A. Eddi, E. Fort, and Y. Couder, Interaction of two walkers: Wave-mediated energy and force, Phys. Rev. E **90**, 063017 (2014).

[18] M. Durey and P. A. Milewski, Faraday wave-droplet dynamics: Discrete-time analysis, J. Fluid Mech. **821**, 296 (2017).

[19] J. Moláček and J. W. M. Bush, Drops walking on a vibrating bath: towards a hydrodynamic pilot-wave theory, J. Fluid Mech. **727**, 612 (2013).

[20] V. Prost, J. Quintela, D. M. Harris, P.-T. Brun, and J. W. M. Bush, *Proceedings of the 68th Annual Meeting of the APS Division of Fluid Dynamics* (APS, Ridge, 2015), Vol. 60, No. 21, http://meetings.aps.org/link/BAPS.2015.DFD.M33.2.

[21] See Supplemental Material at http://link.aps.org/supplemental/10.1103/PhysRevFluids.3.013604 for videos. Video 1 shows a pair of walkers in the $N = 1$ promenade mode, strobed at nearly the bouncing frequency. A colored striped transparent film between the lighting source and bath facilitates visualization of surface deformations. Video 2 shows walkers in the $N = 1$ promenade mode. Left video: Walkers execute the $(2,1)^2$ bouncing mode at forcing acceleration $\gamma/\gamma_F = 0.90 \pm 0.01$. Right video: Walkers execute a $(4,2)$ bouncing mode at forcing acceleration $\gamma/\gamma_F = 0.96 \pm 0.01$.

[22] A. U. Oza, R. R. Rosales, and J. W. M. Bush, A trajectory equation for walking droplets: Hydrodynamic pilot-wave theory, J. Fluid Mech. **737**, 552 (2013).

[23] D. M. Harris and J. W. M. Bush, Generating uniaxial vibration with an electrodynamic shaker and external air bearing, J. Sound Vib. **334**, 255 (2015).

[24] D. M. Harris, T. Liu, and J. W. M. Bush, A low-cost, precise piezoelectric droplet-on-demand generator, Exp. Fluids **56**, 83 (2015).

[25] G. Pucci, D. M. Harris, L. M. Faria, and J. W. M. Bush, Walking droplets interacting with single and double slits, J. Fluid Mech. **835**, 1136 (2018).

[26] Ø. Wind-Willassen, J. Moláček, D. M. Harris, and J. W. M. Bush, Exotic states of bouncing and walking droplets, Phys. Fluids **25**, 082002 (2013).

[27] J. Moláček and J. W. M. Bush, Drops bouncing on a vibrating bath, J. Fluid Mech. **727**, 582 (2013).

[28] M. Couchman (private communication).

[29] A. U. Oza, D. M. Harris, R. R. Rosales, and J. W. M. Bush, Pilot-wave dynamics in a rotating frame: On the emergence of orbital quantization, J. Fluid Mech. **744**, 404 (2014).

[30] L. M. Delves and J. N. Lyness, A numerical method for locating the zeros of an analytic function, Math. Comput. **21**, 543 (1967).

[31] A. U. Oza, Ø. Wind-Willassen, D. M. Harris, R. R. Rosales, and J. W. M. Bush, Pilot-wave hydrodynamics in a rotating frame: Exotic orbits, Phys. Fluids **26**, 082101 (2014).

[32] M. Labousse, S. Perrard, Y. Couder, and E. Fort, Self-attraction into spinning eigenstates of a mobile wave source by its emission back-reaction, Phys. Rev. E **94**, 042224 (2016).

[33] D. M. Harris and J. W. M. Bush, Drops walking in a rotating frame: From quantized orbits to multimodal statistics, J. Fluid Mech. **739**, 444 (2014).

[34] M. Labousse, A. U. Oza, S. Perrard, and J. W. M. Bush, Pilot-wave dynamics in a harmonic potential: Quantization and stability of circular orbits, Phys. Rev. E **93**, 033122 (2016).

[35] L. D. Tambasco, D. M. Harris, A. U. Oza, R. R. Rosales, and J. W. M. Bush, The onset of chaos in orbital pilot-wave dynamics, Chaos **26**, 103107 (2016).